



# Low- $J$ Transitions in $\tilde{A}^2\Pi(0, 0, 0) - \tilde{X}^2\Sigma^+(0, 0, 0)$ Band of Buffer-gas-cooled CaOH

Yuiki Takahashi<sup>1</sup> , Masaaki Baba<sup>2,3</sup>, Katsunari Enomoto<sup>4</sup>, Ayami Hiramoto<sup>5</sup>, Kana Iwakuni<sup>6</sup>, Susumu Kuma<sup>7</sup> ,  
Reo Tobaru<sup>5</sup>, and Yuki Miyamoto<sup>5</sup>

<sup>1</sup> Division of Physics, Mathematics, and Astronomy, California Institute of Technology, Pasadena, CA 91125, USA

<sup>2</sup> Department of Chemistry, Graduate School of Science, Kyoto University, Kyoto 606-8502, Japan

<sup>3</sup> Molecular Photoscience Research Center, Kobe University, Kobe 657-8501, Japan

<sup>4</sup> Department of Physics, University of Toyama, Toyama 930-8555, Japan

<sup>5</sup> Research Institute for Interdisciplinary Science, Okayama University, Okayama 700-8530, Japan; [miyamo-y@cc.okayama-u.ac.jp](mailto:miyamo-y@cc.okayama-u.ac.jp)

<sup>6</sup> Institute for Laser Science, University of Electro-Communications, 1-5-1 Chofugaoka, Chofu, Tokyo 182-8585, Japan

<sup>7</sup> Atomic, Molecular and Optical Physics Laboratory, RIKEN, 2-1 Hirosawa, Wako, Saitama 351-0198, Japan

Received 2022 June 24; revised 2022 August 3; accepted 2022 August 7; published 2022 September 6

## Abstract

Calcium monohydroxide radical (CaOH) is receiving an increasing amount of attention from the astrophysics community as it is expected to be present in the atmospheres of hot rocky super-Earth exoplanets as well as interstellar and circumstellar environments. Here, we report the high-resolution laboratory absorption spectroscopy on low- $J$  transitions in  $\tilde{A}^2\Pi(0, 0, 0) - \tilde{X}^2\Sigma^+(0, 0, 0)$  band of buffer-gas-cooled CaOH. In total, 40 transitions out of the low- $J$  states were assigned, including 27 transitions that have not been reported in previous literature. The determined rotational constants for both ground and excited states are in excellent agreement with previous literature, and the measurement uncertainty for the absolute transition frequencies was improved by more than a factor of 3. This will aid future interstellar, circumstellar, and atmospheric identifications of CaOH. The buffer-gas-cooling method employed here is a particularly powerful method to probe low- $J$  transitions and is easily applicable to other astrophysical molecules.

*Unified Astronomy Thesaurus concepts:* [Molecular spectroscopy \(2095\)](#); [High resolution spectroscopy \(2096\)](#); [Laboratory astrophysics \(2004\)](#); [Experimental techniques \(2078\)](#); [Spectral line lists \(2082\)](#); [Line positions \(2085\)](#)

## 1. Introduction

Calcium monohydroxide molecules ( $^{40}\text{Ca}^{16}\text{O}^1\text{H}$ ) now have a special standing because of their expected presence in the atmospheres of hot rocky super-Earth exoplanets (Bernath 2009; Rajpurohit et al. 2013; Tennyson & Yurchenko 2017). Determining accurate spectroscopic parameters and transition frequencies on relatively simple molecules present in this environment are necessary for exploration of hot rocky super-Earths. Because of highly abundant Ca atoms, CaOH could also be found in interstellar and circumstellar spaces, where the temperature is sometimes in the 10 s of kelvin regime. In fact, CaOH has been detected in cool stellar atmospheres at low spectral resolution (Rajpurohit et al. 2016). CaOH is therefore an excellent spectroscopic target species.

The recent measured active rotational-vibrational energy levels (MARVEL) algorithm (Császár et al. 2007; Furtenbacher et al. 2007; Furtenbacher & Császár 2012; Tóbiás et al. 2019) has provided a data set of rovibronic (rotation-vibration-electronic) transition frequencies and energy levels of CaOH (Wang et al. 2020). It evaluated all available spectroscopic data on CaOH from the published literature at the time (Hilborn et al. 1983; Bernath & Kinsey-Nielsen 1984; Bernath 1985; Coxon et al. 1991, 1992; Jarman & Bernath 1992; Li & Coxon 1992; Ziurys et al. 1992; Scurlock et al. 1993; Coxon et al. 1994; Li & Coxon 1995; Ziurys et al. 1996; Dick et al. 2006). The uncertainty of final MARVEL data is typically  $\geq 0.005 \text{ cm}^{-1}$  (150 MHz), and as there is an absence of experimental transition frequency values in the

literature,  $J=1/2$  energy levels in the  $\tilde{X}^2\Sigma$  ground vibrational state is missed.<sup>8</sup> Low- $J$  transitions are generally more difficult to characterize with high accuracy at room temperature due to the lower population and, therefore, lower sensitivity. Hence, recent high-level ab initio calculations used  $J=3/2$  state data for the adjustment of parameters of potential energy surfaces (Owens et al. 2021).

Several experimental studies have measured the rovibronic spectrum of  $\tilde{A}^2\Pi(0, 0, 0) - \tilde{X}^2\Sigma^+(0, 0, 0)$  band of CaOH. Previous experiments (Hilborn et al. 1983; Bernath 1985; Steimle et al. 1992; Dick et al. 2006) conducted high-resolution spectroscopy using either heated gas or a supersonic jet. Kozyryev et al. (2019) has reported the transition frequency from  $J=3/2$  state employing the buffer-gas-cooling (BGC) (Maxwell et al. 2005; Hutzler et al. 2012; Takahashi et al. 2021) method with an uncertainty of  $\sim 0.03 \text{ cm}^{-1}$ .

The cryogenic BGC is a powerful method to produce cold molecules in a large quantity, regardless of the reactivity and complexity of the target species. Using this method, a variety of cold molecular species have been produced and explored in a range of spectroscopy (Messer & De Lucia 1984; Santamaria et al. 2016; Spaun et al. 2016; Porterfield et al. 2019), as well as precision measurement studies for fundamental physics (Andreev et al. 2018), and laser cooling of molecules (McCarron 2018; Tarbutt 2018). At the Doyle group at Harvard, cold and ultracold experiments have been conducted on CaOH utilizing low- $J$  transitions for laser slowing, cooling, and trapping (Kozyryev et al. 2019; Baum et al. 2020, 2021). In fact, the 3D magneto-optical trapping and subsequent sub-Doppler cooling of buffer-

Original content from this work may be used under the terms of the [Creative Commons Attribution 4.0 licence](#). Any further distribution of this work must maintain attribution to the author(s) and the title of the work, journal citation and DOI.

<sup>8</sup> Note that the transitions out of this state have been previously observed for Stark splitting measurements (Steimle et al. 1992).

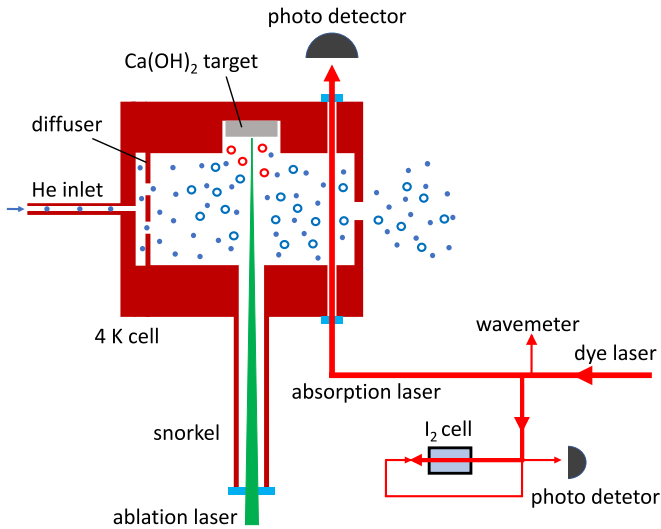


**Figure 1.** Experimental setup for high-resolution spectroscopy of buffer-gas-cooled CaOH. The buffer-gas cell bore is cylindrically symmetric. The blue circle shows the helium buffer-gas atom whereas red (blue) rings indicate hot (cold) CaOH molecules. The red line indicates the laser path emitted from the ring dye laser. The thickness of the lines indicate the laser power although it is not scaled. Note that the structure of the diffuser is simplified for easier readability.

gas-cooled CaOH has been recently achieved using BGC as a precooling technique (Vilas et al. 2022). From the spectroscopic point of view, the BGC technique is especially suitable for probing low- $J$  transitions because the molecular population is moved into lower- $J$  levels, drastically enhancing the sensitivity. Since the BGC technique relies on a mechanism different from the standard methods, such as a supersonic jet, to cool the samples, it can serve as a complementary technique to explore species that are challenging to probe using the standard methods, e.g., larger and more complex molecules (Spaun et al. 2016; Changala et al. 2019; Miyamoto et al. 2022).

In this study, we explore high-resolution laboratory absorption spectroscopy of the  $\tilde{A}^2\Pi(0, 0, 0) - \tilde{X}^2\Sigma^+(0, 0, 0)$  transition of CaOH in a cold buffer-gas cell. The BGC method enables us to probe low- $J$  transitions with small Doppler broadening and high sensitivity. A combination of BGC and corecorded Doppler-free  $I_2$  spectra allows the accurate determination of transition frequencies with an uncertainty of  $<30$  MHz, an improvement of more than three times over previous studies.

## 2. Experimental Apparatus

The cryogenic buffer-gas source for high-resolution spectroscopy on CaOH is shown in Figure 1. The pulsed Nd:YAG laser (532 nm wavelength,  $\sim 10$  ns wide,  $\sim 20$  mJ energy, and 10 Hz repetition rate) is focused on and ablates a solid  $\text{Ca}(\text{OH})_2$  powder target inside a copper cell to produce cold CaOH molecules. The diameter of the focused ablation laser beam at the target is  $\sim 100 \mu\text{m}$ . The body of the buffer-gas cell is made of a copper block with a cylindrical cavity (5 cm long and 2.5 cm diameter). An ablation laser beam is sent through a hole at the center of the cell (2.5 cm from the exit aperture). Similarly, a small hole with windows at approximately 1 cm from the exit aperture provides optical access for the absorption probe laser beam. The copper block is partially extruded to create a long hole in the ablation laser propagation direction (so-called “Snorkel”), shown in Figure 1. This reduces the amount of ablation dust building up on the ablation window.

The buffer-gas cell is attached to the 4 K stage of a pulse tube refrigerator (PTR; Sumitomo Heavy Industries SRP-062B) and held at  $\sim 5$  K. The inlet tube for helium buffer gas is thermally anchored to the 4 K stage of the PTR to ensure precooling to  $\sim 5$  K before entering the cell. Helium buffer gas is introduced from the inlet tube at the back of the cell and then passes through a diffuser at 3 mm from the gas inlet to further ensure good thermalization with the cell wall. The typical flow rate of helium buffer gas is  $\sim 20$  sccm. The helium buffer gas collides with and quickly thermalizes the ablated molecules, eventually leaving the cell through the exit aperture (5 mm diameter). Activated charcoal is attached on the interior surface of the 4 K radiation shields to cryo-pump buffer-gas helium that comes out from the cell, maintaining a high vacuum (typically  $\sim 10^{-5}$  Torr while helium is flowing). The whole system is warmed up to the room temperature roughly every 5–7 days of active operation to release the gas trapped in the charcoal. The typical timescale of cooling down or warming up the system is  $\sim 12$  hr. The ability to easily attach and detach the target holder with screws allows quick powder target swapping. The powder target used in this work is commercially available. A single target with a size of  $\sim 1$  cm diameter yields  $10^4$ – $10^5$  shots. The signal size gradually decays when the ablation spot is unchanged, which is common in other species as well (Iwata et al. 2017).

All measurements in this work were performed on the molecules inside the buffer-gas cell, as opposed to the extracted molecular beam from the cell because of higher molecule density in the cell. A ring cavity dye laser (Coherent 899 dye laser, output power  $\sim 500$  mW, bandwidth  $\sim 1$  MHz) is used to excite the  $\tilde{A}^2\Pi(0, 0, 0) - \tilde{X}^2\Sigma^+(0, 0, 0)$  transition of CaOH whose wavelength is  $\sim 625$  nm. The laser beam is then divided into three parts: a wavemeter,  $I_2$  Doppler-free saturated absorption spectroscopy, and the main experiment (buffer-gas cell). The wavemeter (HighFinesse, WS6-200) has an absolute accuracy of 200 MHz. The absolute frequency is obtained by comparing the corecorded  $I_2$  spectra with the  $I_2$  atlas (Kato et al. 2000) and interpolating the lower and higher calibrated frequencies of each line. The absorption probe laser with a power of  $\sim 100 \mu\text{W}$  and a diameter of  $\sim 1$  mm is sent perpendicular to the direction of the flow of the molecular cloud toward the exit aperture to mitigate the systematic Doppler shift (indicated as a red line in Figure 1).

## 3. Results

A typical averaged absorption signal as a function of time from the ablation ( $t=0$ ) is shown in the inset of Figure 2. After the rapid increase from  $t=0$  to 2 ms, the signal gradually decreases with a long tail of  $>10$  ms. The time window for the time-integrated absorption signal is 500 ns, peaking at  $t=0.8$  ms. The narrow time window is chosen to make the signal less sensitive to the molecule flow dynamics that may exist in the cell. The typical in-cell CaOH density is  $10^8$ – $10^9 \text{ cm}^{-3}$  and shot-by-shot variation in signal size is around a factor of a few. Relatively slow signal decay, with the timescale of  $\sim 10$  s (with 10 Hz repetition rate of ablation), is also present for each target spot. The ablation laser position is therefore changed every  $\sim 100$  s (1000 shots).

Figure 2 shows a typical Doppler-broadened absorption spectra. Transitions without spin-rotation splitting such as  $R_1(J)$ ,  $R_{21}(J)$ , and transitions from the rotational ground state can be observed as isolated peaks (Figure 2 (a)). Other transitions split due to the spin-rotation interaction, which is partially unresolved in the

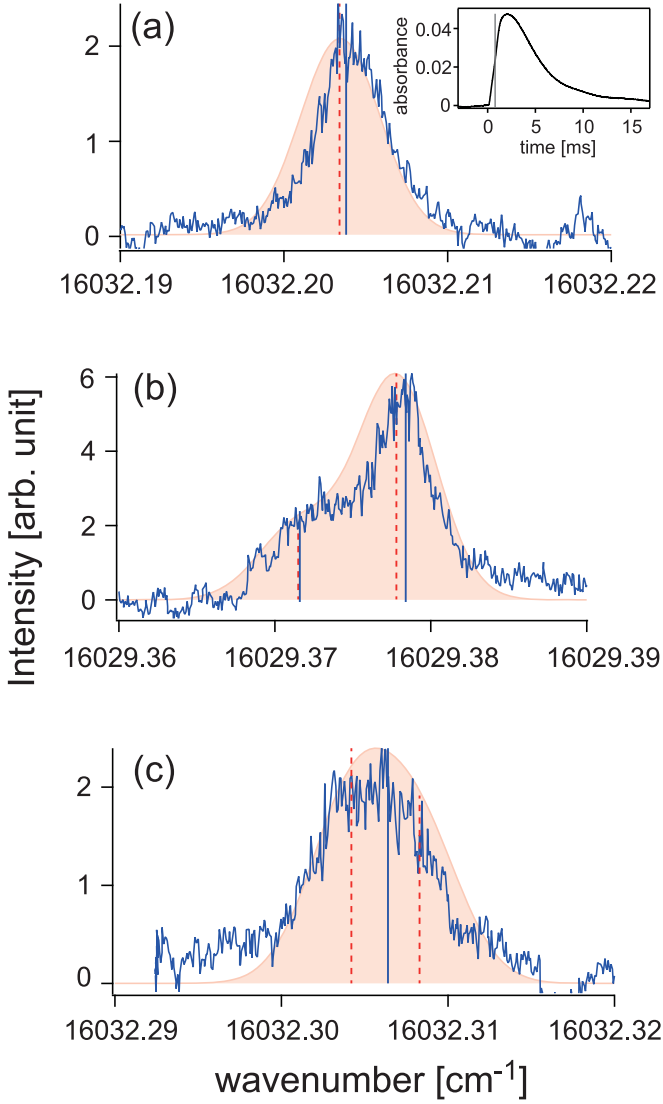


**Figure 2.** Typical Doppler-broadened temporal absorption signal (inset) and spectra in three cases: (a) a single peak in an isolated region, (b) two partially-resolved spin-rotation components ( $Q_2(9/2)$  and  $P_{21}(11/2)$ ), and (c) two unresolved spin-rotation components ( $Q_{21}(7/2)$  and  $R_2(5/2)$ ). The solid gray line in the inset indicates the integration time window. The red dashed (solid blue) lines indicate the fitted (observed) positions. The red area shows the simulated spectrum from the fit results at a translational temperature of 14 K.

present experiment due to Doppler width. As the splitting is comparable to the Doppler width, the resolved lines were also observed as shoulders (Figure 2 (b)). When the spin-rotation splitting is unresolved (Figure 2 (c)), the observed peak is fitted with a single Gaussian, and two spin-rotation components are assigned to the same observed line. The weaker transitions are ignored if the intensity ratio of unresolved transition pairs in the simulation at 10 K is less than one third. The two components obtained by the fitting are usually on both sides of the observed transition. The line residuals are smaller than the transition linewidth. In total, 30 peaks for both  $\Omega = 1/2$  and  $\Omega = 3/2$  spin-orbit components are recorded. Two spin-orbit components are roughly spaced by 66 cm<sup>-1</sup>. The linewidth of each line is about 170 MHz, which corresponds to the Doppler width at 14 K. Due to the shot-by-shot fluctuation in signal size, precise determination

**Table 1**  
Observed Transitions in the  $\tilde{A}^2\Pi(0, 0, 0) - \tilde{X}^2\Sigma^+(0, 0, 0)$  Band of CaOH

Lines	$J''$	Observed	Obs-Calc	Dick et al. (2006)	Difference	
$P_1$	3/2	15964.3929	0.0009	15964.38 <sup>a</sup>	0.0129	
	5/2	15964.0968	0.0017	15964.091	0.0058	
	7/2	15963.8114	0.0028	15963.811	0.0004	
$P_{21}$	11/2	16029.3716	0.0001			
	$Q_1$	1/2	15965.0168	0.0002		
		3/2	15965.3445	0.0009		
		5/2	15965.6821	0.0011		
		7/2	15966.0308	0.0020		
9/2		15966.3899	0.0028			
$Q_2$	13/2	15967.1383	0.0035			
	3/2	16030.1986	-0.0007			
	5/2	16029.9076	-0.0008	16029.933	-0.0254	
	7/2	16029.6344	-0.0001	16029.661	-0.0266	
	9/2	16029.3784	0.0006	16029.383	-0.0046	
$Q_{12}$	1/2	15964.3929	-0.0009			
	3/2	15964.0968	-0.0012			
	5/2	15963.8114	-0.0013			
	$Q_{21}$	3/2	16031.5352	0.0010		
		5/2	16031.9119	0.0012		
7/2		16032.3064	0.0022			
9/2		16032.7144	-0.0005			
11/2		16033.1421	-0.0004			
$R_1$	1/2	15966.1017	-0.0005			
	3/2	15967.1521	-0.0008			
	5/2	15968.2129	-0.0011			
	7/2	15969.2854	0.0000			
	$R_2$	1/2	16031.5352	-0.0008		
3/2		16031.9119	-0.0017	16031.931	-0.0191	
5/2		16032.3064	-0.0019	16032.327	-0.0206	
7/2		16032.7199	-0.0002	16032.734	-0.0141	
9/2		16033.1486	-0.0003	16033.163	-0.0144	
$R_{12}$	3/2	15965.6821	-0.0018			
	5/2	15966.0308	-0.0021			
	7/2	15966.3899	-0.0024			
	11/2	15967.1383	-0.0041			
	$R_{21}$	1/2	16032.2038	0.0004		
3/2		16033.2485	-0.0001			
5/2		16034.3106	-0.0002	16034.328	-0.0174	
7/2		16035.3909	0.0009	16035.406	-0.0151	
9/2		16036.4876	0.0013	16036.502	-0.0144	

**Note.** The frequency unit is in wavenumber (cm<sup>-1</sup>). The  $\Delta J_F F''$  notation is used for specifying transitions.

<sup>a</sup> This value is from Kozyryev et al. (2019).

of rotational temperature is difficult, although the intense low- $J$  transitions suggest an approximate rotational temperature of 10 K.

The frequency is corrected with Doppler-free I<sub>2</sub> spectra, whose uncertainties are less than  $\sim 10$  MHz (Kato et al. 2000). The fitting errors of the CaOH spectra with a Gaussian function are also less than  $\sim 10$  MHz. Statistical uncertainty was estimated to be  $< 20$  MHz by measuring each transition multiple times. One of the possible systematic errors is Doppler shift due to the flow of molecular clouds in the cell. In the previous simulation, the flow velocity toward the cell aperture is  $\sim 10$  m s<sup>-1</sup> (Takahashi et al. 2021). To get a conservative estimate, if we assume that the flow of  $\sim 10$  m s<sup>-1</sup> is in the direction opposite to the laser beam, a shift of 16 MHz occurs. To investigate this systematic error, we checked the line

**Table 2**  
Determined Spectroscopic Constants.

State	Constant	This Work	Dick et al. (2006)	Difference
$\tilde{X}^2\Sigma^+$	$B''$	0.334315(60)	0.334334107(32)	$-1.9107 \times 10^{-5}$
$\tilde{A}^2\Pi$	$T_0$	15997.76559(44)	15997.77579(64)	-0.0102
	$B'$	0.341195(53)	0.3412272(15)	$-3.22 \times 10^{-5}$
	$A'$	66.81849(53)	66.81480(89)	0.00369
	$p'$	-0.04469(23)	-0.0431(71)	-0.001626

**Note.** The numbers in the parentheses indicate the fitting errors. The frequency unit is in wavenumber ( $\text{cm}^{-1}$ ).

positions using the probe absorption laser sent in the opposite direction. We found that the shift depends on the delay from ablation and is less than 15 MHz at 0.8 ms after the ablation. One of the possible explanations for this shift is the molecule flow dynamics in the cell. This systematic effect can be eliminated by using a technique of sending lasers from both directions, e.g., saturated absorption spectroscopy. More detailed investigations on the cause of this error source will be included in a separate paper. Combined with the fitting error and uncertainty from multiple measurements, we estimated the total uncertainty of measurement to be  $<30$  MHz. This is an improvement in measurement uncertainty by more than a factor of three compared to Li & Coxon (1995) and Dick et al. (2006).<sup>9</sup>

The  $I_2$  corrected transition wavenumbers and assignments are given in Table 1 with fit results from the PGOPHER program (Western 2017). For the transition designation, a traditional  $\Delta J_{F'F''}(J'')$  notation was used (Herzberg 1950). A least-squares fit of the measured data to Hund's case (b)  $\tilde{X}^2\Sigma^+$ , Hund's case (a)  $\tilde{A}^2\Pi$ , and Hamiltonian of Brown was performed in the PGOPHER program. Because low- $J$  transitions have a small dependency on higher-order spectroscopic constants, centrifugal distortion constants  $D''$  and  $D'$ , spin-rotation constant  $\gamma''$ ,  $\Lambda$ -type doubling constant  $q'$ , and higher-order spin-orbit constant  $A_D'$  were fixed to the previously obtained values (Dick et al. 2006; see the Appendix). The standard deviation of the fitting residual is  $0.0015 \text{ cm}^{-1}$ .<sup>10</sup> As a result, the 30 observed transitions were assigned to the 40 rotational lines due to the unresolved spin-rotation splittings mentioned above. There are 27 transitions that have not been previously reported in the literature and are assigned in this work.

The obtained spectroscopic parameters are shown in Table 2. The determined rotational constants,  $B$ , for both the ground  $\tilde{X}^2\Sigma^+$  and excited  $\tilde{A}^2\Pi$  states are in excellent agreement with previously determined values within 1 MHz. The difference in the band origin  $T_0$  is  $\sim 0.01 \text{ cm}^{-1}$  (300 MHz), which is comparable to the uncertainty of the previous works, but significant for the uncertainty in the present measurement ( $\sim 30$  MHz). This indicates the improvement of the accuracy of the absolute transition frequency values. The difference in the spin-orbit constant  $A'$  is larger than the present measurement uncertainty<sup>11</sup> whereas the  $\Lambda$ -type doubling constant  $p'$  is comparable.

<sup>9</sup> The uncertainty in Dick et al. (2006) was estimated as “0.005  $\text{cm}^{-1}$  (150 MHz) for clean lines and 0.02  $\text{cm}^{-1}$  (600 MHz) for overlapped lines.”

<sup>10</sup> The fitting residual is limited by roughly the spin-rotation splitting because it is partially unresolved as explained above. If we only select out spin-rotationally resolved lines, the standard deviation of the fit residual reduces to  $\sim 0.0006 \text{ cm}^{-1}$  (18 MHz).

<sup>11</sup> Not to be confused with the fitting error.

## 4. Conclusion

Using the BGC method, laboratory high-resolution spectra of the  $\tilde{A}^2\Pi(0, 0, 0) - \tilde{X}^2\Sigma^+(0, 0, 0)$  band of CaOH were recorded. We assigned a total of 40 low- $J$  transitions, 27 of which do not exist in previous literature. Rotational constants were determined for both  $\tilde{A}^2\Pi(0, 0, 0)$  and  $\tilde{X}^2\Sigma^+(0, 0, 0)$  states and are consistent with previous measurements. In contrast, the experimental uncertainty for the absolute frequencies of low- $J$  transitions was improved by more than a factor of 3. The transition frequencies along with spectroscopic constants obtained in this work are expected to contribute to the MARVEL analysis as an additional data set, aiding in the identification of interstellar, circumstellar, and atmospheric CaOH. The ability to cool the molecular species down to a kelvin regime with the BGC method would also be useful for probing low- $J$  transitions of other astrophysical molecules, especially in an interstellar environment where the temperature can be as cold as a few kelvins. It can also be combined with microwave spectroscopy (Porterfield et al. 2019) to probe the low temperature chemical reactions, opening up a new path to study chemistry in the interstellar medium.

We acknowledge many helpful discussions and kind cooperation from Yosuke Takasu, Satoshi Uetake, Nick Hutzler, Christian Hallas, Louis Baum, Ben Augenbraun, Yoshiro Takahashi, and John Doyle. Y.T. was supported by the Masason Foundation. This work was supported by the Masason Foundation and JSPS KAKENHI grant Nos. 18H01229, 22H01249.

## Appendix: Fixed Parameters in the Fit

All the spectroscopic constants fixed in the fit are listed in Table 3.

**Table 3**  
Fixed Spectroscopic Constants in the Fit.

State	Constant	Fixed Value
$\tilde{X}^2\Sigma^+$	$D''$	$3.86 \times 10^{-7}$
	$\gamma''$	0.00115957
$\tilde{A}^2\Pi$	$D'$	$3.896 \times 10^{-7}$
	$q'$	$-3.447 \times 10^{-6}$
	$A_D'$	$-1.741 \times 10^{-4}$

**Note.** The constants are fixed to the obtained values in Dick et al. (2006). The frequency unit is in wavenumber ( $\text{cm}^{-1}$ ).

## ORCID iDs

Yuiki Takahashi  <https://orcid.org/0000-0003-0027-0556>  
 Susumu Kuma  <https://orcid.org/0000-0003-3120-2572>  
 Yuki Miyamoto  <https://orcid.org/0000-0002-0567-6881>

## References

- Andreev, V., Ang, D. G., DeMille, D., et al. 2018, *Natur*, **562**, 355  
 Baum, L., Vilas, N. B., Hallas, C., et al. 2021, *PhRvA*, **103**, 043111  
 Baum, L., Vilas, N. B., Hallas, C., et al. 2020, *PhRvL*, **124**, 133201  
 Bernath, P., & Kinsey-Nielsen, S. 1984, *CPL*, **105**, 663  
 Bernath, P. F. 2009, *IRPC*, **28**, 681  
 Bernath, P. F., & Brazier, C. R. 1985, *ApJ*, **288**, 373  
 Changala, P. B., Weichman, M. L., Lee, K. F., Fermann, M. E., & Ye, J. 2019, *Sci*, **363**, 49  
 Coxon, J., Li, M., & Presunka, P. 1994, *JMoSp*, **164**, 118  
 Coxon, J. A., Li, M., & Presunka, P. I. 1991, *JMoSp*, **150**, 33  
 Coxon, J. A., Li, M., & Presunka, P. I. 1992, *MolPh*, **76**, 1463  
 Császár, A. G., Czákó, G., Furtenbacher, T., & Mátyus, E. 2007, in *Annual Reports in Computational Chemistry*, ed. D. Spellmeyer & R. Wheeler, Vol. 3 (Amsterdam: Elsevier), 155  
 Dick, M., Sheridan, P., Wang, J.-G., Yu, S., & Bernath, P. 2006, *JMoSp*, **240**, 238  
 Furtenbacher, T., & Császár, A. G. 2012, *JMoSt*, **1009**, 123  
 Furtenbacher, T., Császár, A. G., & Tennyson, J. 2007, *JMoSp*, **245**, 115  
 Herzberg, G. 1950, *Molecular Spectra and Molecular Structure*, Vol. I (2nd edn.; Malabar, FL: Krieger Publishing Company)  
 Hilborn, R. C., Qingshi, Z., & Harris, D. O. 1983, *JMoSp*, **97**, 73  
 Hutzler, N. R., Lu, H.-I., & Doyle, J. M. 2012, *ChRv*, **112**, 4803  
 Iwata, G. Z., McNally, R. L., & Zelevinsky, T. 2017, *PhRvA*, **96**, 022509  
 Jarman, C. N., & Bernath, P. F. 1992, *JChPh*, **97**, 1711  
 Kato, H., Kasahara, S., Misono, M., & Baba, M. 2000, *Doppler-Free High Resolution Spectral Atlas of Iodine Molecule 15000-19000 cm<sup>-1</sup>* (Tokyo: Japan Society for the Promotion of Science)  
 Kozryyev, I., Steimle, T. C., Yu, P., Nguyen, D.-T., & Doyle, J. M. 2019, *NJPh*, **21**, 052002  
 Li, M., & Coxon, J. A. 1992, *JChPh*, **97**, 8961  
 Li, M., & Coxon, J. A. 1995, *JChPh*, **102**, 2663  
 Maxwell, S. E., Brahms, N., DeCarvalho, R., et al. 2005, *PhRvL*, **95**, 173201  
 McCarron, D. 2018, *JPhB*, **51**, 212001  
 Messer, J. K., & De Lucia, F. C. 1984, *PhRvL*, **53**, 2555  
 Miyamoto, Y., Tobaru, R., Takahashi, Y., et al. 2022, arxiv:2206.07927  
 Owens, A., Clark, V. H. J., Mitrushchenkov, A., Yurchenko, S. N., & Tennyson, J. 2021, *JChPh*, **154**, 234302  
 Porterfield, J. P., Satterthwaite, L., Eibenberger, S., Patterson, D., & McCarthy, M. C. 2019, *RSci*, **90**, 053104  
 Rajpurohit, A. S., Reylé, C., Allard, F., et al. 2013, *A&A*, **556**, A15  
 Rajpurohit, A. S., Reylé, C., Allard, F., et al. 2016, *A&A*, **596**, A33  
 Santamaria, L., Sarno, V. D., Natale, P. D., et al. 2016, *PCCP*, **18**, 16715  
 Scurlock, C., Fletcher, D., & Steimle, T. 1993, *JMoSp*, **159**, 350  
 Spaun, B., Changala, P. B., Patterson, D., et al. 2016, *Natur*, **533**, 517  
 Steimle, T. C., Fletcher, D. a., Jung, K. Y., & Scurlock, C. T. 1992, *JChPh*, **96**, 2556  
 Takahashi, Y., Shlivko, D., Woolls, G., & Hutzler, N. R. 2021, *PhRvR*, **3**, 023018  
 Tarbutt, M. R. 2018, *ConPh*, **59**, 356  
 Tennyson, J., & Yurchenko, S. N. 2017, *MolAs*, **8**, 1  
 Tóbiás, R., Furtenbacher, T., Tennyson, J., & Császár, A. G. 2019, *PCCP*, **21**, 3473  
 Vilas, N. B., Hallas, C., Anderegg, L., et al. 2022, *Natur*, **606**, 70  
 Wang, Y., Owens, A., Tennyson, J., & Yurchenko, S. N. 2020, *ApJS*, **248**, 9  
 Western, C. M. 2017, *JQSRT*, **186**, 221  
 Ziurys, L. M., Barclay, W. L. J., & Anderson, M. A. 1992, *ApJL*, **384**, L63  
 Ziurys, L. M., Fletcher, D. A., Anderson, M. A., & Barclay, W. L. 1996, *ApJS*, **102**, 425